On the interaction of stochastic forcing and regime dynamics

Josh Dorrington[1,2] and Tim Palmer[1]

[1]Atmospheric, Oceanic, and Planetary Physics, University of Oxford, Oxford, UK
[2]Institute for Meteorology and Climate (IMK-TRO), Karlsruher Institute of Technology, Germany

Correspondence: Josh Dorrington (joshua.dorrington@kit.edu)

Abstract. Stochastic forcing can, sometimes, stabilise atmospheric regime dynamics, increasing their persistence. This counter-intuitive effect been observed in geophysical models of varying complexity, and here we investigate the mechanisms underlying stochastic regime dynamics in a conceptual model. We use a six-mode truncation of a barotropic β-plane model, featuring transitions between analogues of zonal and blocked flow conditions, and identify mechanisms similar to those seen previously in work on low-dimensional random maps. Namely, we show that a geometric mechanism, here relating to monotonic instability growth, allow for asymmetric action of symmetric perturbations on regime lifetime, and that random scattering can 'trap' the flow in more stable regions of phase space. We comment on the implications for understanding more complex atmospheric systems.

1 Introduction

Rossby (1940) first suggested the atmosphere may possess multiple large-scale quasi-equilibrium states to describe the empirically observed tendency for European weather patterns to take on a finite range of frequently recurrent configurations. These are now known in meteorology as atmospheric regimes, and in dynamical systems such behaviour is known as chaotic intermittency. The first theoretical study of multiple atmospheric equilibria, carried out by Charney and DeVore (1979) (hereafter CdV79) showed that the flow in a low-order mid-latitude barotropic channel could equilibrate to either a zonally symmetric flow or a stationary blocking pattern. They suggested real world equivalents of these equilibria states might be destabilised by perturbations from unresolved modes (in this idealised model, this included spatial scales of $\sim \mathcal{O}(1000)$ km), causing shifts from one state to another and introducing a vacillation between large-scale weather patterns.

Similar results were obtained in other simple models (Charney and Straus, 1980; Kallen, 1981; De Swart, 1988), but these equilibria were often absent in less-truncated systems, rendered 'unrealisable' by shifts in the model attractor or collapsing completely due to structural instability (Reinhold and Pierrehumbert, 1982; Cehelsky and Tung, 1987). Therefore later work moved away from analysis of fixed points, treating regimes as chaotic flows originating from attractor merging (Itoh and Kimoto, 1996, 1997), and exploring the role of homoclinic orbits in preferred transitions between regimes (Kimoto and Ghil, 1993; Kondrashov et al., 2004; Selten and Branstator, 2004).

Despite a deepening mathematical understanding of regimes, the Earth-system appears to be high-dimensional, and as a result linking the regime behaviour of simple models to those of realistic models has proved challenging, especially when further complicated by the introduction of stochastic forcing. Earth-system models often contain explicit stochastic parameterisation

schemes, and in addition a range of small-scale processes that can be thought of as randomly forcing the large-scale flow. Contrary to linear intuition, there is evidence that this fast variability can stabilise regimes: Kwasniok (2014) (hereafter K14) found additive noise increases regime lifetime in both the Lorenz '63 system (Lorenz, 1963) and a chaotic reformulation of the CdV79 model found by Crommelin et al. (2004) (hereafter C04). Further, stochastic forcing has been shown to improve regime predictability by increasing persistence in truncations of the Lorenz '96 model (Düben et al., 2014; Christensen et al., 2015) and climate model regime representation (Dawson and Palmer, 2015), as well as the representation of other slow-varying climate modes (Palmer and Weisheimer, 2011; Berner et al., 2012).

Outside of geoscience, similar stochastic persistence effects have been observed and explained for transient chaotic maps. For transient systems, chaotic dynamics only persist for finite time, eventually "escaping", often to a steady state (Lai and Tél, 2011a). It has been shown for such systems how stochastic forcing can delay the escape of trajectories in the case of 1D (Reimann, 1996; Lai and Tél, 2011b) and 2D (Altmann and Endler, 2010) maps. This is of interest for fully-chaotic geophysical regime systems as the transition between regimes can be conceived of as an escape from one regime to another, and so increases in regime persistence are related to decreases in escape rate. This approach was introduced in Franaszek and Fronzoni (1994) to understand the stochastically forced Duffing oscillator.

We will study the stochastically forced CdV79 model, as retuned by C04, and show that similar mechanisms explain stochastic persistence in this six-dimensional, continuous time, non-hyperbolic regime system as in simpler transiently chaotic maps. We introduce the model and its regime structure in section 2. We then discuss the impact of stochasticity on that regime structure in section 3 and demonstrate that this can be understood as a result of the theory of hitting time problems in combination with a simple geometric mechanism. We summarise our results and discuss the implications for weather and climate in section 4.

2   Model formulation

The deterministic Charney deVore model is obtained by spectral truncation of a barotropic flow in a β-plane channel geometry. It can be expressed as a six-equation system of ordinary differential equations, derived in full in Appendix A:

$$
\begin{aligned}
\dot{x}_1 =& -C(x_1 - x_1^*) + \tilde{\gamma}_1 x_3 \\
\dot{x}_2 =& -Cx_2 + \beta_1 x_3 - \alpha_1 x_1 x_3 - \delta_1 x_4 x_6 \\
\dot{x}_3 =& -Cx_3 - \beta_1 x_2 + \alpha_1 x_1 x_2 + \delta_1 x_4 x_5 - \gamma_1 x_1 \\
\dot{x}_4 =& -C(x_4 - x_4^*) + \epsilon(x_2 x_6 - x_3 x_5) + \tilde{\gamma}_2 x_6 \\
\dot{x}_5 =& -Cx_5 + \beta_2 x_6 - \alpha_2 x_1 x_6 - \delta_2 x_4 x_3 \\
\dot{x}_6 =& -Cx_6 - \beta_2 x_5 + \alpha_2 x_1 x_5 + \delta_2 x_4 x_2 - \gamma_2 x_4
\end{aligned}
\tag{1}
$$

The six variables $\{x_i\}$ represent spectral mode amplitudes of a streamfunction field, subject to a linear relaxation to a zonally symmetric background state, Coriolis and orographic forces, and quadratic advective nonlinearities. To explore stochastic
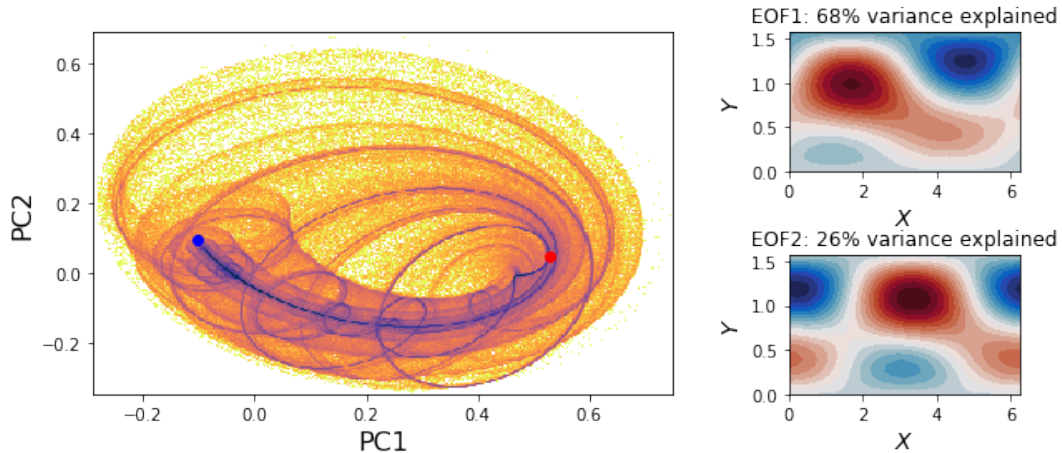
Figure 1. Left: Projection of the deterministic attractor into the space of the leading EOFs, capturing 92% of the total variance. Right: The flow patterns corresponding to the first and second EOFs of the system. Blue and red dots show the positions of fixed points corresponding to blocked and zonal flows respectively.
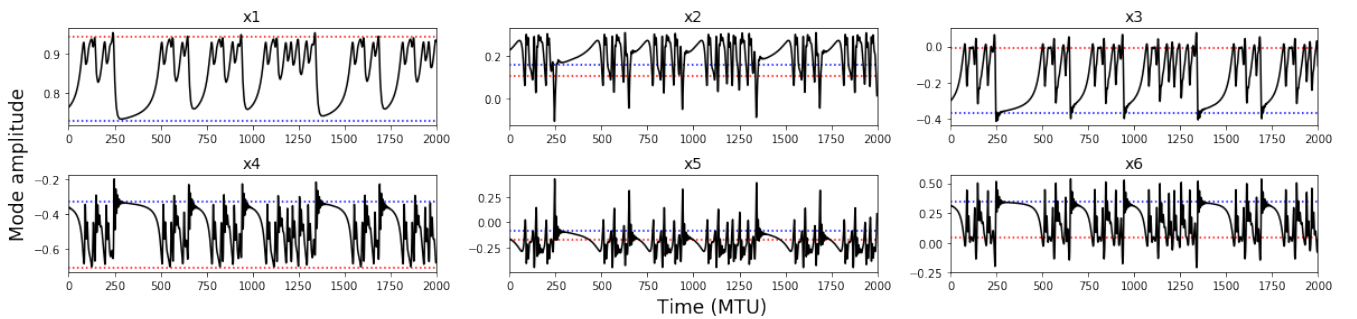
Figure 2. A 2000 MTU integration of the CdV79 system, showing the evolution of each mode amplitude. The dynamics are chaotic but weakly so, showing clear quasiperiodic behaviour. Two regimes of behaviour can be seen; fast chaotic oscillations, divided by periods of slow evolution with irregular duration. The mode values at the blocked and zonal fixed points are shown with dashed blue and red lines.

effects, we introduce an additive white noise vector to the tendency, given by a normal distribution ξ_i with standard deviation σ, as in K14:

$$\dot{x}_i = \dot{x}_{i,\text{Deterministic}} + \sigma \xi_i \tag{2}$$

55

The system is integrated using the Euler-Maruyama difference scheme with a timestep of dt=2e-4 model time units (MTU), and is sampled every 1 MTU. We compute integrations of length 200,000 MTU for a range of σ values.

To visualise the model phase space, we project the six-dimensional attractor into the space of the two leading empirical orthogonal functions (EOFs) of the deterministic system, as shown in figure 1, capturing 94% of the system's variability (figure S1 shows the various projections of the six x-modes). The attractor is highly structured, with a number of strongly preferred trajectories through phase space (note the logarithmic colour scheme in figure 1). This low dimensional attractor shows no obviously separable phase space regions such as the twin lobes of the Lorenz '63 system, and we see that the trajectories are highly twisted together, producing a scroll-like geometry.

A representative sample of the model's temporal evolution is shown in figure 2. Intermittency is readily apparent, with predictable slowly evolving periods, with near-zero phase speed, corresponding to persistent 'blocked' flow patterns, divided by highly chaotic, fast evolving flows that contain both zonally symmetric states and transient wave activity. The regime structure is therefore quite asymmetrical, in contrast to the Lorenz '63 or '96 systems whose regimes are essentially equivalent to eachother. Instabilities in the CdV system arise from two basic mechanisms: an orographically-induced saddle-node bifurcation (a transition from one to multiple fixed-point equilibria) as identified in the original CdV79 paper, and a barotropic Hopf bifurcation (a transition from a fixed point to a periodic orbit) associated with the onset of a zonally propagating waves in the model domain. Both bifurcations are codimension 1, existing along a surface with one less dimension than the parameter space, and so can in general be found by tuning 1 model parameter. Stable steady state and periodic wave solutions to equation 1 are common for arbitrary sets of model parameters (not shown), while chaotic – and especially multimodally chaotic – solutions are harder to find. In the original formulation of CdV79, two stable fixed points were found, corresponding to a zonally symmetric state, and a 'blocked' flow, with strong wave activity. The model parameters used here, and in C04 and K14, are close to a parameter set where the barotropic Hopf and orographic saddle-node bifurcations merge: one fixed point bifurcates into two fixed points and a limit cycle. This fold-Hopf point has codimension 2, meaning two model parameters must be tuned to obtain it. High codimension bifurcations seem to be of reduced relevance to the real world, representing exceptional states in parameter space. However, the fold-Hopf bifurcation is known to produce a range of lower codimension, and so more relevant, bifurcations at nearby parameter values, including paths to chaotic dynamics (Champneys and Kirk, 2004). Most relevant to us is the generation of homoclinic orbits, a type of bifurcation where orbits stretch from a fixed point back to itself, with an infinite period. These orbits can lead to fully fledged chaotic dynamics and the creation of a strange attractor through intersection with an unstable toroidal limit cycle. At the boundary crisis this creates a 'whirlpool repellor' (Shilnikov et al., 1995) and exactly the scrolling structure seen in figure 1. The two fixed points, analogs of those in CdV79, remain but are now unstable, and at the parameter values chosen here the strange attractor moves between the vicinity of these two fixed points, as seen in figures 1 and 2, shadowing collapsed homoclinic orbits. The flow patterns corresponding to these fixed points are shown in figure S2. See De Swart (1988) and C04 for more details on the bifurcation structure of the model. As a result the regimes of the CdV system are rooted in the dynamics of unstable homoclinic orbits, with close approaches to the unstable fixed point leading to periods of slow evolution, and then rapid 'bursting' to chaotic, more turbulent flow. Such behaviour is seen in other simple atmospheric models (Crommelin, 2002) including the Lorenz 84 model (Shilnikov et al., 1995), and in the dynamics of nonlinear circuits (Pusuluri and Shilnikov, 2018) and neurons (Izhikevich, 2006).

This type of regime behaviour is of a fundamentally different type to that of the archetypal Lorenz '63 system. In Lorenz '63, crisis-induced intermittency creates regime dynamics when the basin of attraction of two attractors merge together, triggering movement between two distinct regimes of fully chaotic behaviour. The Charney deVore system, in contrast, experiences almost deterministic dynamics before drifting away and entering a transient chaotic regime. At an unpredictable later time, the system will once again return to the neighbourhood of the periodic orbit, and reenter the slow-evolving regime. For a recent discussion of the co-existence of predictable and chaotic flow states in atmospheric systems see Shen et al. (2021).

2.1 Regimes in CdV

When studying a multimodal system, bulk metrics such as the mean or variance can obscure the underlying dynamical structure. Therefore it is natural to use a regime framework as a way of partitioning phase space into dynamically distinct regions of interest. Following the approach of K14 we use a hidden Markov model (HMM), to identify qualitatively different dynamical regimes, with the minor methodological change of fitting the HMM to the full six-dimensional state vector, rather than restricting to the x_1-x_4 subspace as in K14. As for most clustering methods, we must make an *a priori* choice of regime number when fitting the HMM. We use three regimes, which were found in K14 to well separate the qualitatively distinct model dynamics, capturing both the persistent quasi-predictable blocking regime, the highly chaotic zonal regime, and the transitions between them. Figure 3a) shows the regions of the deterministic attractor assigned to each regime, and figure S3 shows the corresponding flow patterns. The blocking regime is small in phase space extent, focused on the tightly spiralled trajectories that start close to the blocking fixed point. It clearly separates from the swirling trajectories assigned to the transitional regime. The zonal state contains the very chaotic 'branching' of the attractor into different orbits, and contains the early parts of these orbits until their transition back to blocking becomes unavoidable. Interestingly, these regimes broadly correspond to regions of the attractor with different numbers of unstable dimensions (figure 3b)) supporting our choice of 3 regimes as dynamically appropriate. Our regime assignment also has some similarities to those found in Strommen et al. (2021), which used persistent homology to identify regimes in the CdV system and found a persistent component similar to our blocking state.

For non-zero noise amplitude, $\sigma \neq 0$, we identify regimes in the same way, refitting the HMM for each σ value. This is necessary as while the qualitative shape of the attractor[1] is robust over a range of noise amplitudes, the fine structure seen in figure 1 breaks down and the stochastic simulations experience shifts of probability density closer to the location of the blocking fixed point (shown in figure S4).

Figure 4 shows the temporal evolution of the zonally symmetric x_1 mode, and the phase velocity $v_t = \frac{1}{2}\sqrt{\sum_{i=1}^{6}(x_{i,t+1} - x_{i,t-1})^2}$, for different σ values, coloured by regime assignment. The characteristics of the regimes are broadly preserved even up to σ=1.6e-2: the persistent blocking state has low x_1 values and very low phase velocities, the zonal state has high x_1 values and relatively low phase velocities, while the transitional regime has high x_1 values and high phase velocity. However, for the larger value of σ=3.0e-2, it is apparent that there is no meaningful regime structure remaining: the phase velocity never drops

---

[1]While it is not formally accurate to speak of a model attractor for a stochastic system, we shall continue to do so as a shorthand for the well-converged probability density function of the model.
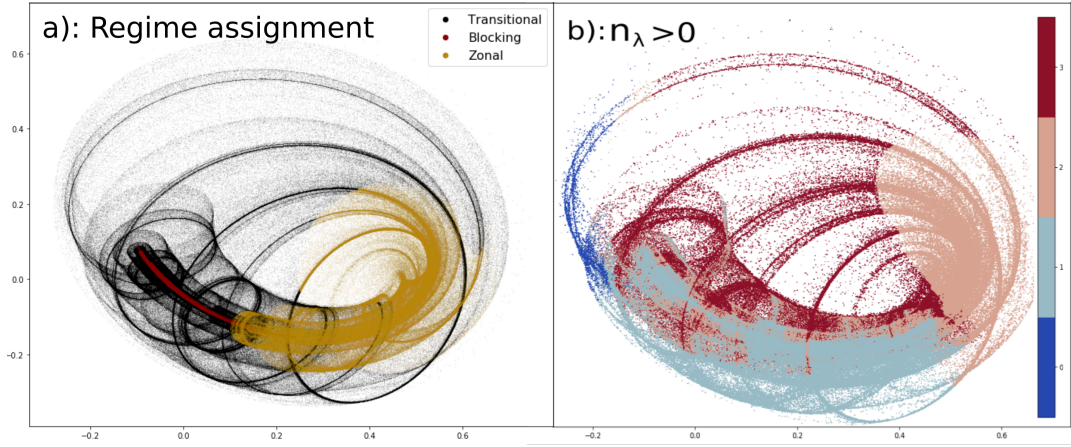
Figure 3. a) The assignment of points on the deterministic model attractor to the three hidden Markov model regimes projected into the EOF1-EOF2 plane. b) the number of unstable dimensions as identified by the positive local Lyapunov exponents, calculated at each point along the deterministic model attractor, projected into the EOF1-EOF2 plane.
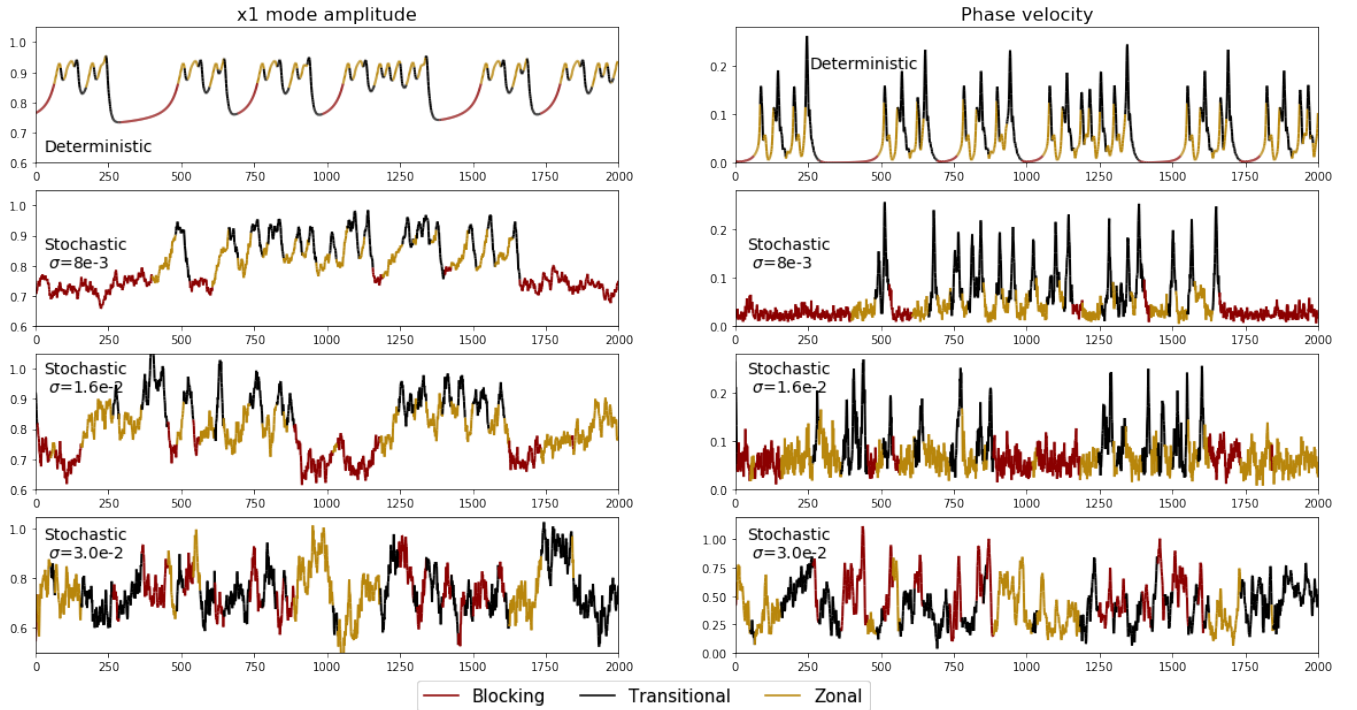
Figure 4. Left: Time evolution of the x_1 mode in deterministic and stochastic cases, with points coloured by their regime assignment. Right: The corresponding phase velocities.
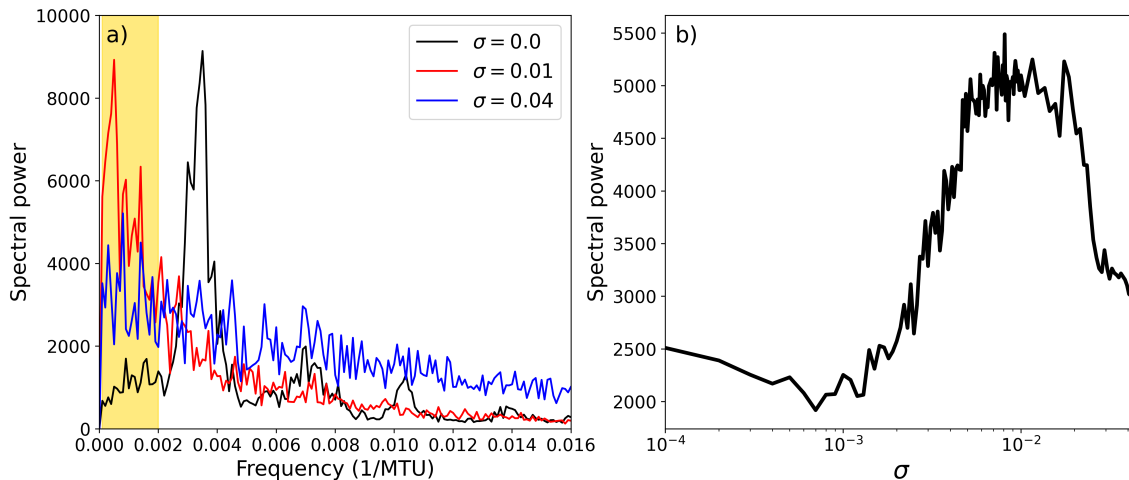
Figure 5. a) The power spectral density of the total mode amplitude, $\sqrt{\sum_i x_i^2}$, for three different strengths of stochastic forcing, σ. b) The spectral power averaged over frequencies from 1/500 MTU^{-1} to 1/10000 MTU^{-1} (corresponding to the shaded region of panel a)) as a function of σ.

below 0.2, indicating a loss of quasistationarity: at this point the deterministic dynamics play second fiddle to the stochastic term, and the assignment of regimes becomes meaningless.

3 Stochastic persistence

Figure 5a) shows Fourier transforms of the total mode amplitude $\sqrt{\sum_i x_i^2}$ for three representative amplitudes of stochastic forcing. The deterministic $\sigma = 0$ spectrum possesses a clear peak consistent with the quasiperiodic nature of the dynamics. For the $\sigma = 0.01$ case this peak has collapsed, producing a flatter spectrum with power shifted towards low frequencies. This is not a monotonic effect: for $\sigma = 0.04$, the total power in the low frequency region decreases, and the spectrum flattens. Figure 5b) shows this non-monotonicity clearly, with a peak in low frequency variability close to $\sigma = 0.01$.

This is in excellent agreement with K14, which showed increasing regime persistence with noise amplitude that peaked at $\sigma = 0.008$ and then decreased. We show here that this is associated with a genuine slowing of the system variables visible in the Fourier spectrum, and is observable independent of adopting a regime perspective. With this reassurance, and given the HMM maintains the same qualitative characteristics for σ values ≤ 0.016, we judge that the regime assignment provides a sensible way to analyse the amplified low frequency variability seen in figure 5 in more detail. Figure 6 shows the distribution of lifetimes for each of the three regimes, as a function of increasing σ. While all regimes show some increase in regime persistence for moderate noise amplitudes, the effect is by far the most significant in the blocking regime, showing a near trebling of mean regime lifetime that peaks at $\sigma = 0.008$. As shown in figure S5, this peak is associated with a 150% increase
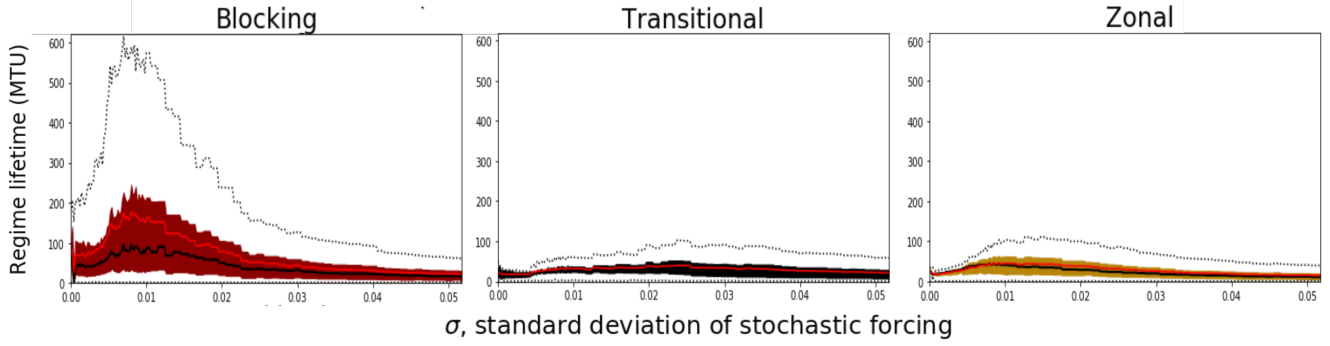
Figure 6. The distribution of blocking regime lifetimes, as a function of stochastic forcing amplitude. Shaded regions mark the interquartile range, with the thick black line showing the median, and the red line the mean. Dotted black lines show the 0th and 95th percentiles of the distribution.
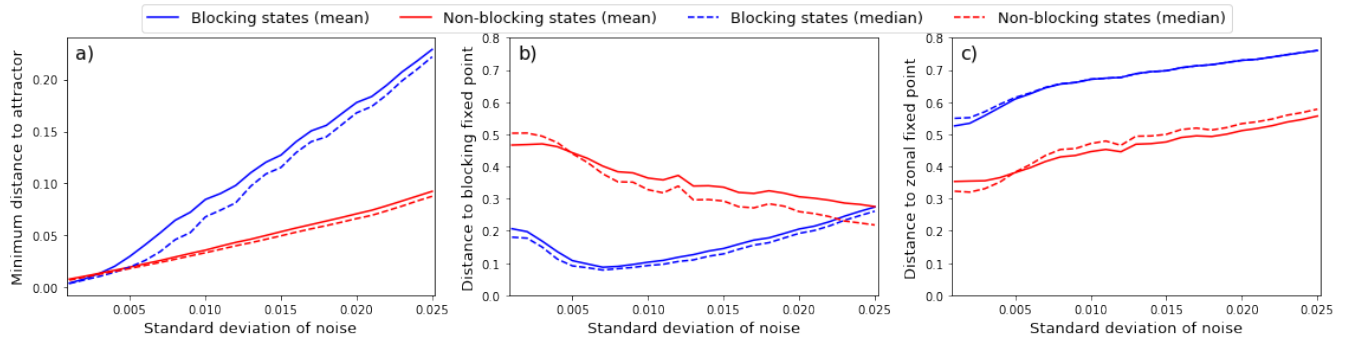
Figure 7. a) The mean (solid lines) and median (dashed lines) euclidean distance between points in the stochastic simulation and their closest neighbour on the deterministic attractor, shown for the blocking and non-blocking regimes. b,c) As in a) but showing the distance between points in each simulation and the blocking (b)) and zonal (c)) equilibria respectively.

in the number of blocks lasting at least 100 MTU, and a 600% increase in those lasting longer than 175 MTU. Changes in
140 the median blocking lifetime are smaller, and the distribution is clearly skewed, with the 95th percentile of blocking lifetime exceeding 600 MTU when persistence is maximum.

How can the ability of random forcing to stabilise regime dynamics be understood? What causes the non-monotonicity between stochastic amplitude and persistence, and why is the response here asymmetric; primarily in the blocking regime? As mentioned, non-monotonic changes of transient lifetime due to stochastic forcing are understood for low-dimensional
145 transiently chaotic maps. Symmetric perturbations can decrease on average the region of phase space in which chaotic transients can 'escape' (i.e. decay) for a large class of 1-D concave maps, lengthening their lifetime (Reimann, 1996; Lai and Tél, 2011b). Additionally, stochasticity smooths the probability density of the deterministic system. If the escape region of the system is
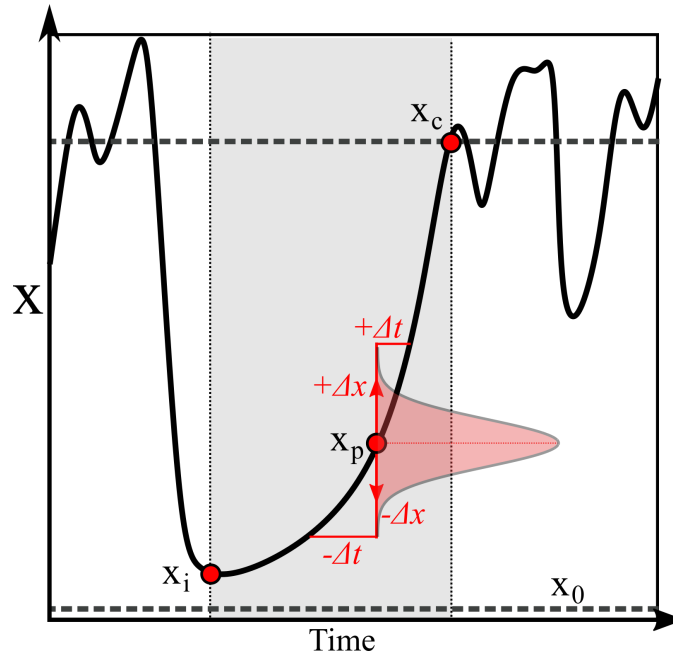
Figure 8. A schematic showing one variable, x, of a chaotic process, which moves between periods of chaotic variability and periods of predictable, monotonic growth (shaded in grey). The predictable regime is entered at a random position x_i, in the neighbourhood of an unstable fixed point x_0, and once it reaches an amplitude x_c it will re-enter the chaotic regime. At a position x_p, we consider the impact of applying a random perturbation Δx to the x variable, drawn from some symmetric probability distribution, with vanishing support outside the interval $[x_p - x_0, x_c - X_p]$. We see that, due to the convex growth of x, a perturbation with negative sign will increase the duration of the predictable period more than a corresponding perturbation with positive sign will shorten it.

of higher than average density, then stochastic forcing can on average knock more trajectories out of this region than in to it, again increasing persistence Altmann and Endler (2010); Faisst and Eckhardt (2003).

150   In our system we first consider the mean state changes. The average distance between points in the stochastic simulations and their closest neighbour on the deterministic attractor increases, approximately linearly, as the amplitude of the stochastic forcing increases (Figure 7a)). Once again there is asymmetry between regimes, with the minimum distance during blocking growing far faster than during the other regimes. Figures 7b) and c) show that this is associated with a drift towards the neighbourhood of the unstable blocking fixed point, with no equivalent result seen for the zonal fixed point (also visible in figure S4). If we

155   consider the dynamics in the neighbourhood of the blocking fixed point, we realise the deterministic tendency there is near-zero, and so the additive stochastic terms dominate entirely: the dynamics approach six-dimensional Brownian motion. How long, in expectation, will it take for this Brownian motion to move the system away from the fixed point once again, and return it to a dynamics-dominated flow state? This question is simply a reformulation of the classic hitting time problem: at what time will a random process first reach a distance a from its initial condition? For Brownian motion in three or more dimensions it

160   is known that in fact the average time taken is infinite: the distribution of hitting times is fat-tailed and so the mean diverges

(Kallenberg, 2017). Therefore the skewed distribution of blocking lifetimes seen in figure 6 can be understood in terms of the amount of time spent near the fixed point, as shown in 7b). As σ increases past 0.008, the average distance from both the attractor *and* the blocking fixed point increases. As the stochastic forcing becomes stronger than the deterministic damping along the stable manifold, the system increasingly explores the full six dimensional phase space, and so the directionality of the forcing vanishes. There is a conceptual similarity here to the second stochastic persistence mechanism of Altmann and Endler (2010) found for mixed phase space systems, whereby trajectories in a 1-D transiently chaotic map can scatter into islands of stability, which introduces a fat tail to the transient lifetime. However, the increased persistence we find is not entirely a result of excursions to the noise-dominated neighbourhood of the fixed point. There is also an important interaction between stochasticity and the low-dimensional, ordered flow of the blocking regime. We present a heuristic mechanism similar in character to that of Lai and Tél (2011b), but now considering a 1D flow as in the schematic figure 8. We can think of this as a parameterisation along the 1D unstable manifold of our CdV79 system moving between a highly chaotic state and a slowly evolving, predictable state. Immediately upon entering the regime of slow evolving dynamics, the system is at a point $x = x_i$ and will stay in the quasi-stationary regime until it reaches $x = x_c$. We assume that x grows monotonically with the time t in this regime, so we can parameterise x in terms of t or vice versa: $f : x \rightarrow t$, $g : t \rightarrow x$. If we let $x = f(t)$ be any convex, monotonic function defined over the interval $[x_0, x_c]$, then $t = g(x) = f^{-1}(x)$, and so g is therefore a concave, monotonic function with negative curvature. We consider applying a single perturbation Δx to the system at a point x_p, drawn from an even probability distribution $P(\Delta x)$ with fast decaying tails and support over $[x_c - x_p, x_p - x_0]$. Informally, this amounts to choosing a point x_p far from the edge of the predictable regime and so there is only a vanishing probability of Δx directly triggering a regime transition. When the standard deviation of P is small compared to $x_c - x_0$, this will apply to most values of x in the interval. From the evenness of P, we see that the impact of the perturbation on the variable x, in expectation, is zero:

$$\langle \Delta x \rangle = 0 \tag{3}$$

However this is not in general the case for $\langle \Delta t \rangle$:

$$\langle \Delta t \rangle = \langle g(x_p + \Delta x) - g(x_p) \rangle = \langle G_p(\Delta x) \rangle \tag{4}$$

where G_p, as a translation of g is also concave. Using the definition of the expectation we find:

$$\langle \Delta t \rangle = \int_{-\infty}^{\infty} G_p(\Delta x) \cdot P(\Delta x) d\Delta x \tag{5}$$

where the limits are justified by our requirement for vanishing tails for P and our choice of x_p.

Because $P(\Delta x)$ is even, then if we Taylor expand G_p we will lose all odd powers on integration and be left with:

$$\langle \Delta t \rangle = \int_{-\infty}^{\infty} \sum_{n=1}^{\infty} \frac{1}{(2n)!} \frac{d^{2n} G_p}{d(\Delta x)^{2n}} \cdot P(\Delta x) d\Delta x \tag{6}$$

And having taken Δx to be small, we can drop high order terms:

$$190 \quad \langle \Delta t \rangle = \int\limits_{-\infty}^{\infty} \frac{1}{2} \frac{d^2 G_p}{d(\Delta x)^2} \cdot P(\Delta x) d\Delta x \tag{7}$$

Because G_p is concave, this derivative is negative and we obtain

$$\langle \Delta t \rangle = - \int\limits_{-\infty}^{\infty} \frac{1}{2} \left| \frac{d^2 G_p}{d(\Delta x)^2} \right| \cdot P(\Delta x) d\Delta x = -I \tag{8}$$

Where I is positive. Therefore any convex perturbation growth will be delayed (i.e. intermittency persisted) by small symmetric random perturbations, *and the average lifetime of the stable regime will increase*. The case for a negatively oriented variable with concave curvature is precisely equivalent, while for a positively oriented variable with concave curvature or a negatively oriented variable with convex curvature decreased persistence would be seen. For the linear case with zero curvature, there is of course no impact of the perturbation on persistence.

When considering the particular case of $f(t) = x_0 e^{\lambda t}$, and $P(\Delta x) = \mathcal{N}(0, \sigma)$, which is interesting for our CdV system, we obtain analytically $\langle \Delta t \rangle = \frac{-\sigma^2}{2\lambda x_p^2}$ (see Appendix B). This quadratic dependence on σ^2 is exactly what is found in Lai and Tél (2011b) and Reimann (1996) for the escape rate for 1D maps . However it is not clear that the two derivations are totally equivalent; we consider a convex monotonic instability, and they a concave non-invertible map. Higher σ corresponds to longer persistence (remembering our overall weak noise approximation), as does small λ, indicating that nearly stable intermittent dynamics can be most substantially persisted. We also see in this case that smaller x_p leads to larger drift, indicating that perturbations soon after the system has entered the intermittent state are most impactful. While we've considered only a single perturbation, the reasoning generalises to a continuous stochastic process, where now the $\langle \Delta t \rangle$ term we have calculated is a spatially dependent drift term. The crux of the argument can be understood solely from examination of figure 8. Any low dimensional, convexly growing instability in the climate system should be susceptible to the same stochastic suppression. We can also see why only the blocking regime showed dramatic persistence increases, as it is the only regime where the variables evolve with a constant sign of curvature, and where there is only one unstable dimension. The decrease of lifetime for larger noise values does not emerge naturally from this framework, but can be understood as entering a noise-dominated regime where the stochastic terms are much larger than the deterministic tendency.

4 Conclusions

In this paper we have investigated the interaction between stochasticity and strongly nonlinear dynamics in a six-equation conceptual model of atmospheric flow. We consider the case of an additive stochastic forcing applied to a chaotic flow which transitions intermittently between chaotic zonal and quasi-stationary blocked regimes, which Kwasniok (2014) showed exhibited stochastically-reinforced regime persistence for a range of noise amplitudes. We have investigated the mechanisms

driving this behaviour, and provide heuristic arguments based on the stochastic suppression of instability growth and random scattering close to an unstable fixed point. The low dimensionality and ordered nature of the blocking regime leads to a slow monotonically growing instability, which will on average be persisted by a random perturbation rather than accelerated. This effect is amplified, and a heavy tail introduced into the lifetime of blocking events, through chance excursions to the neighbourhood of a deterministically inaccessible fixed point, where the overall deterministic tendency is negligible. Here, the dynamics are almost entirely noise-dominated, and the system will remain close to the fixed point until it scatters away. Ultimately, if stochastic forcing is increased past a certain point, persistence decreases. This is not a resonance effect, but is instead a distinct feature exhibited by transient systems and systems near boundary crises (Altmann and Endler, 2010), where a balance must be struck between providing enough diffusion to escape the deterministic transition trajectories, and providing so much diffusion that new purely stochastic routes out of the regime are created. The mechanisms driving stochastic regime dynamics have many similarities to the dynamics of stochastic transiently chaotic maps. Understanding regime transitions as escapes from the neighbourhood of one non-attracting set to another provides a different perspective that makes clear the connection to the theory of stochastically perturbed escape rates. In atmospheric physics more attention is generally paid to continuous time fully-chaotic conceptual models such as the archetypal Lorenz '63 system (Lorenz, 1963), but the study of regime systems may well benefit from a deeper consideration of the framework of transient chaos, and the wealth of work done on discrete-time maps. Indeed, all chaotic systems can be understood in terms of transient shadowing of unstable periodic orbits (P. Cvitanović and R. Artuso and R. Mainieri and G. Tanner and G. Vattay, 2016), and such ideas have been recently applied to blocking flows (Lucarini and Gritsun, 2019) and regime systems (Maiocchi et al., 2022). Characterising the unstable periodic orbits associated with each regime could even allow the non-monotonic dependence of regime lifetime on stochasticity to be analytically computed using perturbative methods (Cvitanović et al., 1999). Understanding the impacts of stochastic parameterisation on truly transient processes, such as mesoscale convective features is also of great importance (Pickl et al., 2022). It remains to be seen however how relevant these simple mechanisms are in more complex atmospheric models, and indeed the impact of stochastic physics on climate model regime structure are still unclear, complicated by high sampling variability in the Euro-Atlantic region (Dorrington et al., 2022). A natural next step is to ask how stochasticity impacts regimes in quasigeostrophic settings, and to explore how the mechanisms uncovered here evolve (or indeed, are rendered extinct) as the complexity of the flow increases. Finally, intermittent dynamical systems such as those possessing circulation regimes are typically close to a bifurcation. Such near-crisis dynamics are particularly sensitive to stochastic forcing, and as we have seen the response of the system to forcing amplitude can be complex. As a further example, Wackerbauer and Kobayashi (2007) demonstrated high sensitivity of the escape rate in a spatiotemporal system on the spatial correlation of the noise process. This highlights the potential importance of carefully selecting the amplitude and kind of stochastic parameterisations in complex models: not all representations of stochasticity in a system can be expected to be equivalently effective.

Appendix A: Derivation of the Charney deVore 1979 model

Here we derived the CdV79 model introduced in section 2 from the shallow water equations, marking simplifying approxi-
mations in **boldface**. The shallow water system is a simple but highly useful model of fluid flow. Consider a **single layer** of
fluid, with **constant density** ρ, **negligible viscosity**, a vertical pressure gradient deriving solely from gravity (i.e. the fluid is
in **hydrostatic equilibrium**), and which, as the name implies, has a representative **horizontal length scale** L **much larger
than the vertical length scale** H. The dynamics of this system are completely determined by the momentum equation and the
mass-conservation equation.

The momentum equation in a rotating frame is given by

$$\frac{\partial \mathbf{v}}{\partial t} + (\mathbf{v} \cdot \boldsymbol{\nabla})\mathbf{v} + \mathbf{f} \times \mathbf{v} = -g\boldsymbol{\nabla}H \tag{A1}$$

while the mass-conservation equation is

$$\frac{\mathrm{D}H}{\mathrm{D}t} + H\boldsymbol{\nabla} \cdot \mathbf{v} = 0 \tag{A2}$$

Where $\mathbf{v}$ is velocity, $\mathbf{f}$ represents Coriolis forces, g is simply the gravitational constant (**assumed constant**) and H is the
depth of the fluid column. Here the mass-conservation simply expresses that if velocities converge at a point, the height of the
fluid column must rise in response. Application of the identity $(\mathbf{a} \cdot \mathbf{b})\mathbf{c} = -\mathbf{a} \times (\mathbf{b} \times \mathbf{c}) + (\mathbf{a} \cdot \mathbf{c})\mathbf{b}$ to equation A1 gives us

$$\frac{\partial \mathbf{v}}{\partial t} + [(\boldsymbol{\nabla} \times \mathbf{v}) \times \mathbf{v} + \frac{1}{2}\boldsymbol{\nabla}v^2] + \mathbf{f} \times \mathbf{v} = -g\boldsymbol{\nabla}H \tag{A3}$$

and by introducing the absolute vorticity $\xi = \boldsymbol{\nabla} \times \mathbf{v}$, and taking the curl of both sides, we get the shallow water vorticity
equation:

$$\frac{\partial \boldsymbol{\xi}}{\partial t} + \boldsymbol{\nabla} \times ((\boldsymbol{\xi} + \mathbf{f}) \times \mathbf{v}) = 0 \tag{A4}$$

Again, we apply the triple product identity and the chain rule and find:

$$\frac{\partial \boldsymbol{\xi}}{\partial t} + (\mathbf{v} \cdot \boldsymbol{\nabla})(\boldsymbol{\xi} + \mathbf{f}) + (\boldsymbol{\xi} + \mathbf{f})(\boldsymbol{\nabla} \cdot \mathbf{v}) = 0 \tag{A5}$$

Where $\boldsymbol{\nabla} \cdot \boldsymbol{\xi} = \boldsymbol{\nabla} \cdot (\boldsymbol{\nabla} \times \mathbf{v}) = 0$ by definition and $(\boldsymbol{\xi} \cdot \boldsymbol{\nabla})\mathbf{v} = 0$ because $\boldsymbol{\xi}$, as a curl of horizontal wind, does not project onto
the variability of $\mathbf{v}$. Indeed, at this point we note that both $\boldsymbol{\xi}$ and $\mathbf{f}$ have no horizontal components, and so we focus only on the
scalar equation for the z-component, letting $\xi := \xi_z$ and $f := f_z$ for convenience. The divergent velocity term can be rewritten
with the aid of equation A2 by rearranging:

$$\boldsymbol{\nabla} \cdot \mathbf{v} = \frac{-1}{H}\frac{\mathrm{D}H}{\mathrm{D}t} \tag{A6}$$

and substituting into equation A5. This leaves us with

$$\frac{\mathrm{D}\left(\xi+f\right)}{\mathrm{D}t} - \frac{\left(\xi+f\right)}{H}\frac{\mathrm{D}H}{\mathrm{D}t} = 0 \tag{A7}$$

275   which can be put into a clearer form using the chain rule:

$$\frac{\mathrm{D}}{\mathrm{D}t}\left[\frac{\left(\xi+f\right)}{H}\right] = 0 \tag{A8}$$

That is, the potential vorticity $q = \frac{\xi+f}{H}$ is materially conserved. If the thickness of the fluid increases, then the absolute vorticity must likewise increase, due to the stretching of the flow.

We divide our fluid height H into some average fluid depth D and an anomaly component $h(x,y)$ describing the height
280   of surface orography, so that $H = D - h(x,y)$. We assume **shallow orography** so we may take the limit where $\frac{h}{D} << 1$ and
Taylor expand H, truncating at first order so that $\frac{1}{H} \approx \frac{1}{D} + \frac{h}{D^2}$:

$$\frac{\mathrm{D}}{\mathrm{D}t}\left[\xi+f+\frac{(\xi+f)h(x,y)}{D}\right] = 0 \tag{A9}$$

In the midlatitude atmosphere this is a reasonable approximation at the largest scales. For example, if we let D be the height
of the tropopause – around 8 km – and we let h be the average elevation of Europe or North America – between 500 and 800
285   metres – then the limit holds. We also choose to place ourselves in the **quasigeostrophic limit** of low Rossby number, where
$\xi < f$. Finally, we take a β **plane approximation** to the Coriolis force, and this brings us to the barotropic vorticity equation
in the presence of shallow orography:

$$\frac{\mathrm{D}}{\mathrm{D}t}\left[\xi+\beta y+\frac{f_0}{D}h(x,y)\right] = 0 = \frac{\mathrm{D}q}{\mathrm{D}t} \tag{A10}$$

We define $\gamma = \frac{f_0}{D}$ and introduce the streamfunction Ψ, given by $u = -\frac{\partial\Psi}{\partial y}$, $v = \frac{\partial\Psi}{\partial x}$, $\xi = \nabla^2\Psi$. We also generalise slightly
290   by introducing an external source (or sink) of vorticity F. Writing our material derivative out explicitly, we now have:

$$\frac{\partial\nabla^2\Psi}{\partial t} - \frac{\partial\Psi}{\partial y}\cdot\frac{\partial}{\partial x}[\nabla^2\Psi+\gamma h+\beta y] + \frac{\partial\Psi}{\partial x}\cdot\frac{\partial}{\partial y}[\nabla^2\Psi+\gamma h+\beta y] = F \tag{A11}$$

Or more concisely

$$\frac{\partial\nabla^2\Psi}{\partial t} + \mathcal{J}(\Psi,\nabla^2\Psi+\gamma h) - \beta\frac{\partial\Psi}{\partial x} = F \tag{A12}$$

Where the Jacobian operator is given by

295   $$\mathcal{J}(A,B) := \frac{\partial A}{\partial x}\frac{\partial B}{\partial y} - \frac{\partial B}{\partial x}\frac{\partial A}{\partial y} \tag{A13}$$

Taking our **forcing to be a linear relaxation** towards a background state, we now have our explicit equation for the evolution of Ψ:

$$\frac{\partial}{\partial t}\boldsymbol{\nabla}^2\Psi = -J(\Psi, \boldsymbol{\nabla}^2\Psi + \gamma h) - \beta\frac{\partial\Psi}{\partial x} - C(\Psi - \Psi^*) \tag{A14}$$

This is the CdV79 equation, before spectral truncation, where Ψ^* is our background streamfunction. We consider the flow in a **channel geometry**, with periodic boundary conditions in the zonal direction, and with no-penetration and no-slip conditions in the meridional direction. Of course the real atmosphere has no hard meridional boundaries; however the impacts of the subtropical and midlatitude jets have been shown to produce a waveguiding effect that meridionally confines low-frequency variability in a similar way, both in low-order models (Hoskins and Ambrizzi, 1993; Yang et al., 1997) and in observations (Branstator, 2002), which makes this a reasonable first approximation.

We consider a channel of dimensionless zonal length $x = [0, 2\pi]$, and meridional length $y = [0, b\pi]$, so that b then is a free parameter controlling the shape of the channel.

A1 Discretising the model

To convert this infinite dimensional partial differential equation into a system of ordinary differential equations, we can use a Galerkin projection. This involves expanding our spatially dependent variables (Ψ, Ψ^*, and h) in terms of an infinite linear sum of complete spatial basis functions, labelled $\{\Phi(x,y)_i\}$:

$$\Psi(x,y,t) = \sum_i^\infty \Psi_i(t)\Phi_i(x,y) \tag{A15}$$

$$\Psi^*(x,y) = \sum_i^\infty \Psi_i^*\Phi_i(x,y) \tag{A16}$$

$$h(x,y) = \sum_i^\infty h_i\Phi_i(x,y) \tag{A17}$$

We start by defining this basis abstractly, requiring the basis functions to be eigenfunctions of the Laplacian operator and the zonal derivative:

$$\nabla^2\Phi_i = -a_i^2\Phi_i \tag{A18}$$

$$\frac{\partial\Phi}{\partial x} = b_i\Phi_i \tag{A19}$$

The Jacobian term is the thorniest point in the spectral analysis, as it non-linearly mixes spectral modes together. It is the impact of this term that prevents an arbitrary spectral truncation of equation A14 being a solution of the full equation. In full generality, we simply consider that the Jacobian of each pair of basis functions has some projection on every other basis function:

$$J(\Phi_j, \Phi_k) = c_{ijk}\Phi_i \tag{A20}$$

The projection coefficient of the jth and kth modes on the ith mode, c_{ijk}, is computable simply through a direct pointwise product of the ith mode and the Jacobian, integrated over the domain and appropriately normalised:

$$c_{ijk} = \frac{\int_0^{2\pi}\int_0^{b\pi}\Phi_i J(\Phi_j,\Phi_k)dydx}{\int_0^{2\pi}\int_0^{b\pi}dydx} \tag{A21}$$

Under these constraints, we can now rewrite equation A14 projected onto the ith basis function as:

$$\frac{\partial}{\partial t}\Psi_i = \beta a_i^{-2}b_i\Psi_i - C(\Psi_i - \Psi_i^*) - \sum_{j,k}a_i^{-2}c_{ijk}(a_k^2\Psi_j\Psi_k - \gamma\Psi_j h_k) \tag{A22}$$

Where the double sum indexes over all basis functions. We make an explicit choice of basis functions now, taking a Fourier basis defined as:

$$\begin{cases} \sqrt{2}\cos\left(\frac{ny}{b}\right) & \text{if } m=0 \\ \sqrt{2}e^{imx}\sin\left(\frac{ny}{b}\right) & \text{else} \end{cases}$$

where the meridional mode $n > 0$ and the zonal mode m can take any non-integer value. It is easy to verify that these basis functions satisfy the boundary conditions and eigenfunction constraints defined above. To actually solve these spectrally transformed equations, it will be necessary to introduce a truncation, disregarding wave modes exceeding a cutoff wavenumber. Here we choose to introduce a zonal threshold of $|m| \leq 1$ and a meridional threshold of $n \leq 2$, **restricting us to just 6 basis functions**, as in CdV79, C04 and K14.

Although up to this point our approximations have been well motivated physically, we cannot rigorously justify introducing such a drastic truncation without resorting to self-interest: such a system is much easier to study, and can be understood in more detail than a high-dimensional model. Nonetheless, we may reason that any phenomena observed in this truncated model, which will have to derive solely from the dynamics of the largest scales, may have analogues in the true atmospheric circulation, although there they will be shaped and influenced by coupling to smaller scales. The resulting basis functions are shown in figure A1.

Concretely, while the true spectral equation for the largest wave modes, equation A22, contains an infinite number of nonlinear coupling terms, after truncation we are reduced to only 36 such terms, representing only interactions between the resolved modes: the ability for small scales to feed vorticity into the untruncated large scales is neglected.
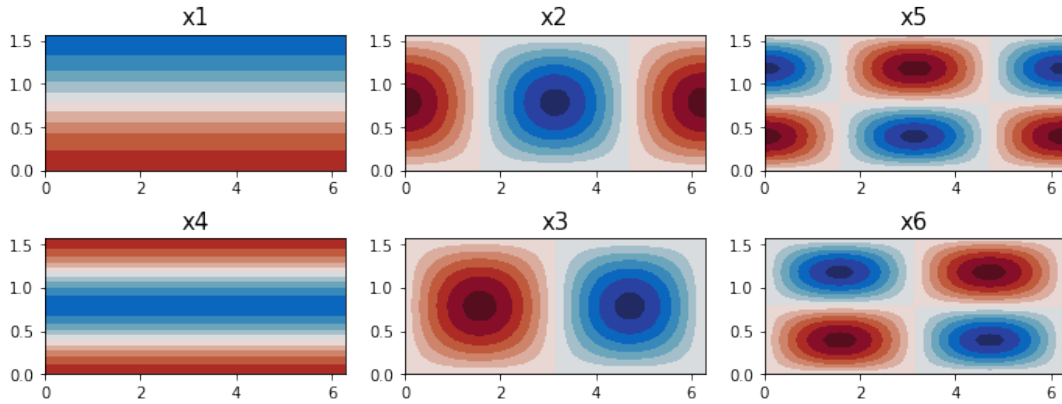
Figure A1. The real-valued basis functions used in the spectrally truncated CdV79 system, plotted as streamfunctions
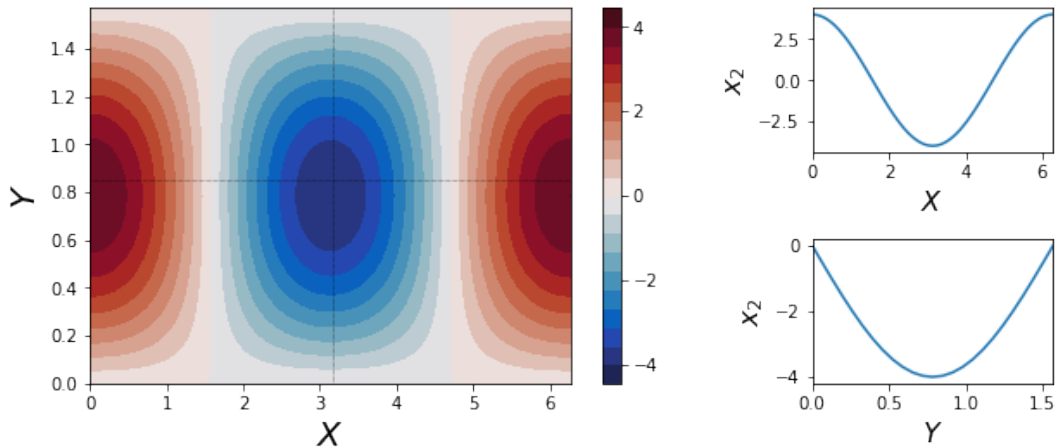
Figure A2. The orographic profile used in the CdV79 system, with a trough in the centre of the domain and a ridge over the periodic boundary. Sub-panels show cross sections across the domain, following the dotted black lines.

We choose our **linear relaxation to be zonally symmetric**, representing the forcing effect of the pole-to-equator temperature gradient. We choose our orography to include a single peak straddling the periodic boundary, with a trough in the centre of the domain. $h(x, y) = \gamma\sqrt{2}\cos(x)\sin\left(\frac{y}{b}\right)$ (this is shown in figure A2).

Obtaining the coefficients in A22 is now simply a matter of calculating integrals, but is very involved, and is best performed using symbolic computation software (an implementation using sympy (Meurer et al., 2017) can be found at https://github.com/joshdorrington/Thesis_materials/blob/main/10d_mode_derivation.ipynb). After computing coefficients, we now diverge slightly from CdV79, transforming our variables to a real basis, as in C04, given by:

$$x_1 = \tfrac{1}{b}\Phi_{0,1} \qquad\qquad x_4 = \tfrac{1}{b}\Phi_{0,2}$$
$$x_2 = \tfrac{1}{\sqrt{2}b}(\Phi_{1,1}+\Phi_{-1,1}) \quad x_3 = \tfrac{i}{\sqrt{2}b}(\Phi_{1,1}-\Phi_{-1,1})$$
$$x_5 = \tfrac{1}{\sqrt{2}b}(\Phi_{1,2}+\Phi_{-1,2}) \quad x_6 = \tfrac{i}{\sqrt{2}b}(\Phi_{1,2}-\Phi_{-1,2})$$

This transformation is purely cosmetic; the behaviour of the system is unchanged. At the end of this process we obtain an explicit six-equation system:

$$\dot{x}_1 = -C(x_1 - x_1^*) + \tilde{\gamma}_1 x_3$$

$$\dot{x}_2 = -Cx_2 + \beta_1 x_3 - \alpha_1 x_1 x_3 - \delta_1 x_4 x_6$$

$$\dot{x}_3 = -Cx_3 - \beta_1 x_2 + \alpha_1 x_1 x_2 + \delta_1 x_4 x_5 - \gamma_1 x_1$$

$$\dot{x}_4 = -C(x_4 - x_4^*) + \epsilon(x_2 x_6 - x_3 x_5) + \tilde{\gamma}_2 x_6 \tag{A23}$$

$$\dot{x}_5 = -Cx_5 + \beta_2 x_6 - \alpha_2 x_1 x_6 - \delta_2 x_4 x_3$$

$$\dot{x}_6 = -Cx_6 - \beta_2 x_5 + \alpha_2 x_1 x_5 + \delta_2 x_4 x_2 - \gamma_2 x_4$$

Where colours encode the linear relaxation, Coriolis forces, orographic impacts and non-linear advection. We see that there are far less than the 36 promised non-linear terms per equation: most quadratic interactions integrated over the domain vanish due to symmetry considerations. $\{\alpha_n\}, \{\beta_n\}, \{\delta_n\}, \{\gamma_n\}, \{\tilde{\gamma}_n\}$ and ϵ are simple geometric constants of $\mathcal{O}(1)$ given in C04.

There are now a number of dimensionless free parameters in the model, which we set equal to the values used in K14 and C04:

- x_i^*: The forcing vector, representing thermal relaxation towards a background state. We use a zonally symmetric forcing profile with $x_1 = 0.95, x_4 = -0.76095$, all other terms zero (shown in figure A3).

- C: The thermal relaxation timescale. Set to $C = 0.1$, describing a damping time of ~ 10 days.

- γ: The orographic amplitude. Set to $\gamma = 0.2$, corresponding to a 200-metre amplitude.

- β: The Coriolis parameter. Set to $\beta = 1.25$, defining a central latitude of $45°$.

- b: Defines the channel half-width. Set to $b = 0.5$, which gives a channel of 6300 km x 1600 km
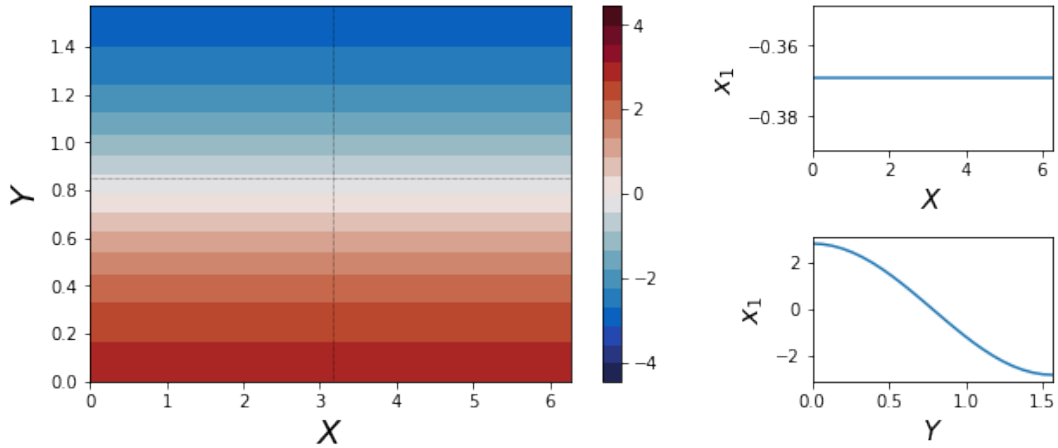
Figure A3. The background state in the Crommelin '04 formulation of the CdV system. It is zonally symmetric and represents the impact of the meridional temperature gradient. Again, sub-panels show cross sections across the domain, following the dotted black lines.

Appendix B: Impact of a Gaussian perturbation on exponential growth

In section 3 we found that

$$\langle \Delta t \rangle = -\int_{-\infty}^{\infty} \frac{1}{2} \left| \frac{d^2 G}{d(\Delta x)^2} \right| \cdot P(\Delta x) d\Delta x = -I \tag{B1}$$

370   If we consider x to be undergoing exponential growth, and subject it to a Gaussian perturbation so that $x = f(t) = x_0 e^{\lambda t}$, and $P(\Delta x) = \mathcal{N}(0, \sigma)$, then we can obtain an analytical form for Δt. Remembering that $G_p(\Delta x) = g(x_p + \Delta x) - g(x_p)$, and seeing that $g(x) = \frac{1}{\lambda} \log\left(\frac{x}{x_0}\right)$, we have:

$$\langle \Delta t \rangle = \int_{x_0}^{x_c} \frac{1}{\lambda} \log\left(\frac{x}{x_p}\right) \cdot \frac{1}{\sigma\sqrt{2\pi}} e^{-\frac{1}{2}\left(\frac{x-x_p}{\sigma}\right)^2} dx \tag{B2}$$

     We transform our variables to $w = \frac{\Delta x}{\sigma} = \frac{x - x_p}{\sigma}$, which implies $\frac{x}{x_p} = \frac{x_p + \sigma w}{x_p} = 1 + \frac{\sigma}{x_p}w$ and $dx = \sigma \cdot dw$. Our limits of
375   integration become $w_0 = \frac{x_0 - x_p}{\sigma} < 0$ and $w_c = \frac{x_c - x_p}{\sigma} > 0$.

     If, as in the main text, we assume σ is small relative to a typical length scale of x (that is the perturbation is vanishingly unlikely to force the system into the chaotic regime directly) then these limits will be very large in absolute magnitude. Given this and the exponentially decaying tails of the Gaussian distribution, we approximate $w_0 \approx -\infty$, $w_c \approx +\infty$. This gives us:

$$\langle \Delta t \rangle = \frac{1}{\lambda\sqrt{2\pi}} \int_{-\infty}^{+\infty} \log\left(1 + \frac{\sigma}{x_p}w\right) \cdot e^{-\frac{w^2}{2}} dw \tag{B3}$$

While not directly integrable, we can make progress by Taylor expanding the logarithm. Firstly we recognise that as the Gaussian distribution is even in w, then all odd terms in the Taylor expansion will vanish. Secondly we note that $\frac{\sigma}{x_p}w = \frac{\Delta x}{x_p}$ will be small if, as above, σ is small, so we can drop terms of 4th order and higher in w. Thus we end up with:

$$\langle \Delta t \rangle = \frac{-\sigma^2}{2\lambda x_p^2 \sqrt{2\pi}} \int\limits_{-\infty}^{+\infty} w^2 \cdot e^{-\frac{w^2}{2}}\, dw \tag{B4}$$

Which, from any book of identities, we can find gives:

$$\langle \Delta t \rangle = \frac{-\sigma^2}{2\lambda x_p^2 \sqrt{2\pi}} \cdot \sqrt{2\pi} = \frac{-\sigma^2}{2\lambda x_p^2} \tag{B5}$$

Author contributions. JD performed all simulations and drafted the manuscript, under the supervision of TP

Acknowledgements. The authors would like to thank Glenn Shutts, Daan Crommelin and Frank Kwasniok for enlightening discussions. We would like to thank one anonymous reviewer and Tamás Bódai for valuable feedback that has helped to strengthen the manuscript considerably.

References

Altmann, E. G. and Endler, A. (2010). Noise-enhanced trapping in chaotic ccattering. *Physical Review Letters*, 105(24):244102.

Berner, J., Jung, T., and Palmer, T. N. (2012). Systematic Model Error: The Impact of Increased Horizontal Resolution versus Improved Stochastic and Deterministic Parameterizations. *Journal of Climate*, 25(14):4946–4962.

Branstator, G. (2002). Circumglobal Teleconnections, the Jet Stream Waveguide, and the North Atlantic Oscillation. Technical Report 14.

Cehelsky, P. and Tung, K. K. (1987). Theories of multiple equilibria and weather regimes - a critical reexamination. Part II: baroclinic two-layer models. *Journal of the Atmospheric Sciences*.

Champneys, A. R. and Kirk, V. (2004). The entwined wiggling of homoclinic curves emerging from saddle-node/Hopf instabilities. *Physica D: Nonlinear Phenomena*, 195(1-2):77–105.

Charney, J. G. and DeVore, J. G. (1979). Multiple Flow Equilibria in the Atmosphere and Blocking. *Journal of the Atmospheric Sciences*, 36(7):1205–1216.

Charney, J. G. and Straus, D. M. (1980). Form-drag instability, multiple equilibria and propagating planetary waves in baroclinic, orographically forced, planetary wave systems. *Journal of the Atmospheric Sciences*.

Christensen, H. M., Moroz, I. M., and Palmer, T. N. (2015). Simulating weather regimes: impact of stochastic and perturbed parameter schemes in a simple atmospheric model. *Climate Dynamics*, 44(7-8):2195–2214.

Crommelin, D. T. (2002). Homoclinic Dynamics: A Scenario for Atmospheric Ultralow-Frequency Variability. *Journal of the Atmospheric Sciences*, 59(9):1533–1549.

Crommelin, D. T., Opsteegh, J. D., and Verhulst, F. (2004). A Mechanism for Atmospheric Regime Behavior. *Journal of the Atmospheric Sciences*.

Cvitanović, P., Søndergaard, N., Palla, G., Vattay, G., and Dettmann, C. P. (1999). Spectrum of stochastic evolution operators: Local matrix representation approach. *Physical Review E*, 60(4):3936.

Dawson, A. and Palmer, T. N. (2015). Simulating weather regimes: impact of model resolution and stochastic parameterization. *Climate Dynamics*, 44(7-8):2177–2193.

De Swart, H. E. (1988). Low-order spectral models of the atmospheric circulation: A survey. *Acta Applicandae Mathematicae*, 11(1):49–96.

Dorrington, J., Strommen, K., and Fabiano, F. (2022). Quantifying climate model representation of the wintertime Euro-Atlantic circulation using geopotential-jet regimes. *Weather and Climate Dynamics*, 3(2):505–533.

Düben, P. D., McNamara, H., and Palmer, T. N. (2014). The use of imprecise processing to improve accuracy in weather & climate prediction. *Journal of Computational Physics*, 271:2–18.

Faisst, H. and Eckhardt, B. (2003). Lifetimes of noisy repellors. *Physical Review E*, 68(2):026215.

Franaszek, M. and Fronzoni, L. (1994). Influence of noise on crisis-induced intermittency. *Physical Review E*, 49(5):3888.

Hoskins, B. J. and Ambrizzi, T. (1993). Rossby Wave Propagation on a Realistic Longitudinally Varying Flow. *Journal of the Atmospheric Sciences*, 50(12):1661–1671.

Itoh, H. and Kimoto, M. (1996). Multiple Attractors and Chaotic Itinerancy in a Quasigeostrophic Model with Realistic Topography: Implications for Weather Regimes and Low-Frequency Variability. *Journal of the Atmospheric Sciences*, 53(15):2217–2231.

Itoh, H. and Kimoto, M. (1997). Chaotic itinerancy with preferred transition routes appearing in an atmospheric model. *Physica D: Nonlinear Phenomena*, 109(3-4):274–292.

Izhikevich, E. M. (2006). *Dynamical Systems in Neuroscience: The Geometry of Excitability and Bursting*. MIT Press.

Kallen, E. (1981). The Nonlinear Effects of Orographic and Momentum Forcing in a Low-Order, Barotropic Model. *Journal of the Atmospheric Sciences*, pages 2150–2163.

Kallenberg, O. (2017). *Random Measures, Theory and Applications*, volume 77 of *Probability Theory and Stochastic Modelling*. Springer International Publishing, Cham.

Kimoto, M. and Ghil, M. (1993). Multiple Flow Regimes in the Northern Hemisphere Winter. Part I: Methodology and Hemispheric Regimes. *Journal of the Atmospheric Sciences*, 50(16):2625–2644.

Kondrashov, D., Ide, K., and Ghil, M. (2004). Weather Regimes and Preferred Transition Paths in a Three-Level Quasigeostrophic Model. *Journal of the Atmospheric Sciences*, 61(5):568–587.

Kwasniok, F. (2014). Enhanced regime predictability in atmospheric low-order models due to stochastic forcing. *Philosophical Transactions of the Royal Society A: Mathematical, Physical and Engineering Sciences*, 372(2018):20130286–20130286.

Lai, Y. C. and Tél, T. (2011a). Introduction to Transient Chaos. *Applied Mathematical Sciences (Switzerland)*, 173:3–35.

Lai, Y. C. and Tél, T. (2011b). Noise and Transient Chaos. *Applied Mathematical Sciences (Switzerland)*, 173:107–143.

Lorenz, E. N. (1963). Deterministic nonperiodic flow. *Universality in Chaos, Second Edition*, 20(2):367–378.

Lucarini, V. and Gritsun, A. (2019). A new mathematical framework for atmospheric blocking events. *Climate Dynamics 2019 54:1*, 54(1):575–598.

Maiocchi, C. C., Lucarini, V., and Gritsun, A. (2022). Decomposing the dynamics of the Lorenz 1963 model using unstable periodic orbits: Averages, transitions, and quasi-invariant sets. *Chaos: An Interdisciplinary Journal of Nonlinear Science*, 32(3):033129.

Meurer, A., Smith, C. P., Paprocki, M., Čertík, O., Kirpichev, S. B., Rocklin, M., Kumar, A. T., Ivanov, S., Moore, J. K., Singh, S., Rathnayake, T., Vig, S., Granger, B. E., Muller, R. P., Bonazzi, F., Gupta, H., Vats, S., Johansson, F., Pedregosa, F., Curry, M. J., Terrel, A. R., Roučka, Š., Saboo, A., Fernando, I., Kulal, S., Cimrman, R., and Scopatz, A. (2017). SymPy: Symbolic computing in python. *PeerJ Computer Science*, 2017(1):e103.

P. Cvitanović and R. Artuso and R. Mainieri and G. Tanner and G. Vattay (2016). *Chaos: Classical and Quantum}*. Niels Bohr Inst.

Palmer, T. N. and Weisheimer, A. (2011). Diagnosing the causes of bias in climate models - why is it so hard? Geophysical and Astrophysical Fluid Dynamics*, 105(2-3):351–365.*

Pickl, M., Lang, S. T., Leutbecher, M., and Grams, C. M. (2022). The effect of stochastically perturbed parametrisation tendencies (SPPT) on rapidly ascending air streams. Quarterly Journal of the Royal Meteorological Society*, 148(744):1242–1261.*

Pusuluri, K. and Shilnikov, A. (2018). Homoclinic chaos and its organization in a nonlinear optics model. Physical Review E*, 98(4):040202.*

Reimann, P. (1996). Noisy one-dimensional maps near a crisis. I. Weak Gaussian white and colored noise. Journal of Statistical Physics 1996 82:5*, 82(5):1467–1501.*

Reinhold, B. B. and Pierrehumbert, R. T. (1982). Dynamics of Weather Regimes: Quasi-Stationary Waves and Blocking. Monthly Weather Review*, 110(9):1105–1145.*

Rossby, C. G. (1940). Planetary flow patterns in the atmosphere. Quart. J. Roy. Meteor. Soc. (suppl)*„ (66):68–87.*

Selten, F. M. and Branstator, G. (2004). Preferred Regime Transition Routes and Evidence for an Unstable Periodic Orbit in a Baroclinic Model. Journal of the Atmospheric Sciences*, 61(18):2267–2282.*

Shen, B. W., Pielke, R. A., Zeng, X., Baik, J. J., Faghih-Naini, S., Cui, J., and Atlas, R. (2021). Is weather chaotic? Coexistence of chaos and order within a generalized lorenz model. Bulletin of the American Meteorological Society*, 102(1):E148–E158.*

Shilnikov, A., Nicolis, G., and Nicolis, C. (1995). Bifurcation and predictability analysis of a low-order atmospheric circulation model. International Journal of Bifurcation and Chaos*, 05(06):1701–1711.*

465   Strommen, K., Chantry, M., Dorrington, J., and Otter, N. (2021). *A topological perspective on regimes in dynamical systems.*

Wackerbauer, R. and Kobayashi, S. (2007). *Noise can delay and advance the collapse of spatiotemporal chaos.* Physical Review E - Statistical, Nonlinear, and Soft Matter Physics*, 75(6):066209.*

Yang, S., Reinhold, B., and Källé, E. (1997). *Multiple Weather Regimes and Baroclinically Forced Spherical Resonance.* Journal of the Atmospheric Sciences*, 54(11):1397–1409.*